Giant anisotropy in superconducting single crystals of CsCa$_2$Fe$_4$As$_4$F$_2$

Zhi-Cheng Wang,[1] Yi Liu,[1] Si-Qi Wu,[1] Ye-Ting Shao,[1] Zhi Ren,[2] and Guang-Han Cao[1,3,4,*]

[1]*Department of Physics and Zhejiang Province Key Laboratory of Quantum Technology and Device, Zhejiang University, Hangzhou 310027, China*

[2]*Institute of Natural Sciences, Westlake Institute for Advanced Study, Westlake University, Hangzhou 310064, China*

[3]*State Key Lab of Silicon Materials, Zhejiang University, Hangzhou 310027, China*

[4]*Collaborative Innovation Centre of Advanced Microstructures, Nanjing University, Nanjing 210093, China*

We report the transport and magnetic measurements on single crystals of CsCa$_2$Fe$_4$As$_4$F$_2$, a recently discovered double-FeAs-layer superconductor with $T_c \sim 30$ K. We observed a large resistivity anisotropy of $\rho_c(T)/\rho_{ab}(T) \sim 10^3$ that tends to increase with decreasing temperature. The $\rho_c(T)$ data exhibit a nonmetallic behavior at high temperatures, suggesting an incoherent electronic state due to the dimension crossover. The superconducting onset transition temperature in $\rho_{ab}(T)$ is 0.7 K higher than that in $\rho_c(T)$, reflecting two-dimensional (2D) superconducting fluctuations. The lower and upper critical fields also show an exceptionally high anisotropy among iron-based superconductors. The $H_{c1}^\perp(T)$ data are well fitted with two s-wave-like superconducting gaps, $\Delta_1(0) = 6.75$ meV and $\Delta_2(0) = 2.32$ meV. The interplane coherence length $\xi_c(0)$ is estimated to be 3.6 Å, which is remarkably smaller than the distance between conducting layers (8.6 Å), consolidating the 2D nature in the title material.

I. INTRODUCTION

Fe-based high-temperature superconductors (FeSCs) are structurally characterized by the anti-fluorite-type Fe$_2X_2$ ($X =$ As, Se) layers [1–3] which serve as the superconductingly active motif. The Fe$_2X_2$ layers are either separated by insulating layers (for the "1111"-type compounds), or connected with monatomic layers (for the "122"-type materials), or directly contacted due to van der Waals forces (for the "11"-type system) [2]. Recently we discovered a series of double-Fe$_2$As$_2$-layer FeSCs, AkCa$_2$Fe$_4$As$_4$F$_2$ ($Ak =$ K, Rb, Cs) [4,5] and $AkLn_2$Fe$_4$As$_4$O$_2$ ($Ak =$ K, Rb, Cs; $Ln =$ Nd, Sm, Gd, Tb, Dy, Ho) [6–8], resembling the cuprate superconductors with double CuO$_2$ sheets. Those so-called 12442-type FeSCs are actually resulted from the intergrowth of 1111- and 122-type iron arsenides. Figure 1(a) shows the crystal structure of one of the family members, CsCa$_2$Fe$_4$As$_4$F$_2$ [5], which is also the research object of the present study. As is seen, the Cs$^+$-cations connected double Fe$_2$As$_2$ layers are separated by the insulating Ca$_2$F$_2$ block. Note that the alkali-metal-containing 122 block is nominally hole doped with 0.5 holes/Fe, while the 1111 block is nominally undoped. Consequently, the 12442-type compounds are all hole doped by themselves at a level of 0.25 holes/Fe, which makes them superconducting at $T_c = $ 28–37 K without extrinsic doping [4–8]. In the case of an extrinsic electron doping through Co/Fe substitution, superconductivity gradually disappears, accompanied by a sign change in Hall coefficient [9].

Our previous magnetoresistance measurements on polycrystalline samples of 12442-type superconductors show that the superconducting transition is severely broadened with pronounced tails under external magnetic fields. Consequently, there exists a large gap between the upper critical field $H_{c2}(T)$ and the irreversible field $H_{irr}(T)$ [4–6], suggesting a pronounced vortex-liquid phase because of the layered structure. The first-principles studies [9–12] reveal enhanced two dimensionality. Furthermore, the initial slope of $\mu_0 H_{c2}(T)$ achieves -16.5 T/K for the RbGd$_2$Fe$_4$As$_4$O$_2$ polycrystals [6], which implies small superconducting coherence lengths. So far, all the related works [4–9,13–18] were based on polycrystalline samples. To reveal the intrinsic anisotropic properties, one needs the measurements on single crystals of the 12442-type FeSCs. In this article we report the growth and the anisotropic properties of CsCa$_2$Fe$_4$As$_4$F$_2$ single crystals. A large anisotropy was observed both in the normal state and in the superconducting state, different from the common knowledge of FeSCs with relatively small anisotropy [19–21]. The strongly anisotropic behavior is reminiscence of those of most cuprate superconductors, implying the crucial role of two dimensionality for the superconductivity.

II. EXPERIMENTAL METHODS

Single crystals of CsCa$_2$Fe$_4$As$_4$F$_2$ were grown in the CsAs flux with a molar ratio of CsCa$_2$Fe$_4$As$_4$F$_2$: CsAs $= 1 : 14$. The source materials were Cs ingot (99.5%), Ca shot (99.5%), Fe powders (99.99%), As pieces (99.999%), and CaF$_2$ powders (99%). First, CsAs was prepared by reacting Cs and As in a sealed quartz tube at 200 °C for 10 h. Intermediate products of CaAs and Fe$_2$As were similarly synthesized at 750 °C for 12 h in evacuated quartz tubes, respectively. Then the precursors were mixed with CaF$_2$ at a molar ratio of CsAs : CaAs : Fe$_2$As : CaF$_2$ = 15 : 1 : 2 : 1. The mixtures were

---

*Corresponding author: ghcao@zju.edu.cn
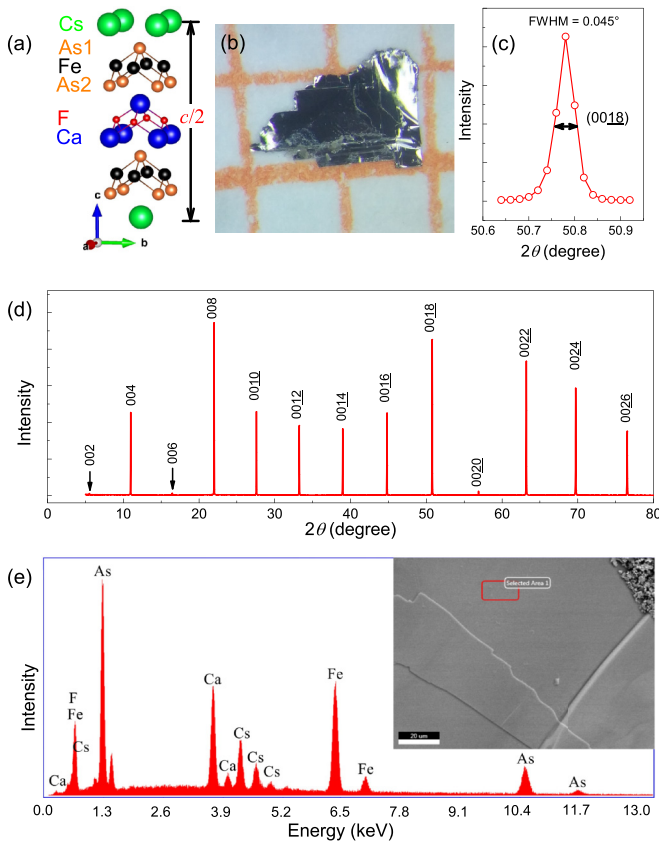
FIG. 1. (a) Crystal structure (only half unit cell is shown) of $CsCa_2Fe_4As_4F_2$ which highlights the insulating Ca_2F_2 layer that separates the superconducting double Fe_2As_2 layers. (b) Photograph of a piece of single crystal on millimeter grid paper. (d) X-ray diffraction pattern (θ-2θ scan) of the $CsCa_2Fe_4As_4F_2$ single crystal showing $(00l)$ reflections with l = even numbers exclusively. (c) A close-up for the $(00\underline{18})$ reflection, from which the full width at half maximum (FWHM) can be seen. (e) The energy dispersive x-ray spectroscopy with the electron beam focus on the rectangular spot of the crystal's surface (see the inset).

loaded in an alumina tube, subsequently sealed in a Ta tube. The Ta tube was jacketed with an evacuated quartz ampoule. The sample-charged assembly was slowly heated to 1150 °C, holding for 20 h. The crystals were expected to nucleate and grow up during the slow cooling down to 800 °C at a rate of 3.75 °C/h. The assembly was then quenched in water at about 800 °C. Finally, shiny platelike crystals [see Fig. 1(b)] were harvested after washing away the CsAs flux with deionized water.

The single crystals were characterized by x-ray diffraction (XRD) on a PANalytical x-ray diffractometer with the Cu$K_{\alpha 1}$ radiation, and by scanning electron microscopy (SEM) on a Hitachi S-4800 equipped with an AMETEK© EDAX (Model Octane Plus) spectrometer. Both θ-2θ scan and θ scan (rocking curves) were performed in the XRD experiments. The $CsCa_2Fe_4As_4F_2$ single crystals can be easily cleaved into thin foils with ordinary adhesive tapes. The resultant SEM images are shown in Fig. S1 of the Supplemental Material (SM) [22]. The measurement of the energy dispersive x-ray spectroscopy [Fig. 1(e)] indicates that the atomic ratios in the

single crystals are basically consistent with the stoichiometry of $CsCa_2Fe_4As_4F_2$ (see Table S1 in the SM for the details).

The anisotropic electrical resistivity measurements were carried out on a Quantum Design Physical Property Measurement System (PPMS-9) adopting a four-terminal method (see the insets of Fig. 3 for the electrode arrangement) and the Montgomery technique (see Fig. S4 in the SM for the details) with an excitation current of 1 mA. The samples were carefully cut and shaped, and the ones chosen for the measurements were $\sim$30 μm in thickness without detectable cleaving and delamination under an optical microscope. The direct-current (dc) magnetization was measured on a Quantum Design Magnetic Property Measurement System (MPMS3) with a crystal whose dimension was $1.2 \times 1.8 \times 0.030$ mm^3 (0.34 mg). Note that the data in the main article were from the same crystalline chunk which was cleaved or cut into several pieces for the different measurements.

III. RESULTS AND DISCUSSION

A. X-ray diffraction

Figure 1(d) shows a typical XRD pattern of the $CsCa_2Fe_4As_4F_2$ single crystal. Only $(00l)$ reflections with l = even numbers appear, consistent with the body centered lattice [5]. One of the diffraction peaks, the $(00\underline{18})$ reflection, is scaled up in Fig. 1(c). One sees that the peak is very sharp with a full width at half maximum (FWHM) as small as $0.045°$, indicating a uniform spacing of the layers. To detect the in-plane structural integrity, we performed the θ-scan measurement. The FWHM value in the resultant rocking curve is somewhat broad ($\sim$1°) and sample dependent, as shown in Fig. S2 of the SM. The specimen's bending (due to its softness) and/or cleaving could account for the sample-dependent peak broadening.

With the measured d spacings corresponding to $(00l)$ diffractions, the c axis is calculated to be 32.331(3) Å by a least squares fit, which is very close, yet slightly smaller than the value of 32.363(1) Å obtained from the powder XRD pattern of the polycrystalline sample [5]. Here we give a plausible explanation. The polycrystalline sample could have slight Cs vacancies due to loss of Cs during the high-temperature sintering. The Cs deficiency corresponds to a higher formal valence of Fe, which would give rise to a higher c/a ratio [23]. As for the single crystals, which were grown in a Cs-rich flux, the Cs vacancies could be minimized. Hence the c value is lower. If this is the case, the hole-doping level in the single crystals is closer to 0.25 holes/Fe, while the previous polycrystalline samples may be overdoped. Indeed, the T_c value of the single crystals is about 2 K higher (see below) than that of the polycrystalline samples.

B. Resistivity

Figure 2(a) shows the temperature dependence of the in-plane (ρ_{ab}) and out-of-plane (ρ_c) resistivity for $CsCa_2Fe_4As_4F_2$ single crystals at zero magnetic field. The configurations of the electrode fabrication can be referred to in the insets of Fig. 3. The $\rho_{ab}(T)$ behavior is quite similar to that of the polycrystalline sample [5], although the latter is about 5 times larger in magnitude. The small anomalies
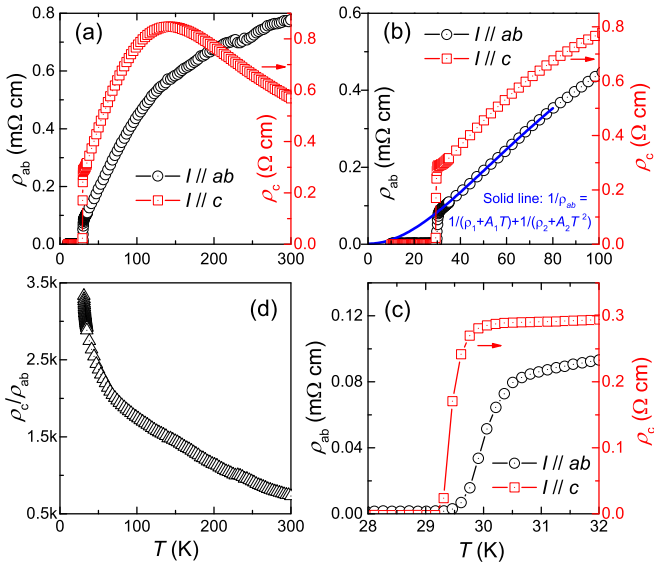
FIG. 2. (a) Temperature dependence of the in-plane (ρ_{ab}, with electric current flowing in the ab plane, left axis) and out-of-plane (ρ_c, with electric current along the c axis, right axis) resistivity of $CsCa_2Fe_4As_4F_2$ single crystals at zero magnetic field. (b) and (c) A close-up in different temperature ranges, respectively. The solid line in (b) is the fitted result using the formula shown (see the text also). (d) The temperature dependence of the anisotropic resistivity ratio ρ_c/ρ_{ab}.

at high temperatures are not intrinsic, likely arising from the incomplete solidification of the silver paste on the sample. There is a gradual change in slope at around 140 K, which commonly appears in hole-doped iron-based superconductors [24]. Below 80 K, the resistivity decreases linearly, suggesting the existence of a non-Fermi-liquid state. However, one notes that the linear fit yields a negative intercept of

$\rho_0 = -0.0836$ mΩ cm, which seems to be unphysical because ρ_0 is normally referred to as a residual resistivity at zero temperature. Given the multiband feature in FeSCs, one may consider a two-fluid model with both non-Fermi liquid and Fermi liquid. According to an extended Matthiessen's rule, the total conductivity ($1/\rho_{ab}$) is contributed from the two fluids, namely,

$$1/\rho_{ab} = 1/(\rho_1 + A_1 T) + 1/(\rho_2 + A_2 T^2), \qquad (1)$$

where ρ_1 and ρ_2 denote the residual resistivity due to different impurity scattering within non-Fermi liquid and Fermi liquid, respectively. The data fitting in the temperature range of $32 < T < 80$ K with Eq. (1) yields $\rho_1 = 0.578(7)$ mΩ cm, $\rho_2 = 0.00126(2)$ mΩ cm, $A_1 = 0.0020(6)$ mΩ cm/K, and $A_2 = 0.000105(3)$ mΩ cm/K². The result avoids any negative residual resistivity. Importantly, the fitted line extrapolated down to low temperatures [see Fig. 2(b)] tends to coincide with the following magnetoresistance data [Fig. 3(c)].

The $\rho_c(T)$ behavior is very different, both in magnitude and in the temperature dependence. The absolute resistivity at room temperature is 570 mΩ cm, 730 times larger then the ρ_{ab} value at 300 K. Plotted in Fig. 2(d) is the resistivity anisotropy ratio $\Gamma_\rho = \rho_c/\rho_{ab}$. One sees that Γ_ρ increases with decreasing temperature, achieving a very large value of about 3150 at $T \to T_c$. To confirm the giant resistivity anisotropy ratio, we measured $\rho_{ab}(T)$, $\rho_c(T)$, and Γ_ρ on different pieces of the crystals and with an additional Montgomery technique. The results (Figs. S3 and S4 in the SM) are basically consistent. The Γ_ρ value is remarkably larger than that ($\sim$100 [25] or $\sim$4 [26]) in $BaFe_2As_2$, and it is comparable to those of the Tl- and Bi-based cuprate superconductors [27,28] and those of the electron-doped iron-selenide superconductors $(Li_{0.84}Fe_{0.16})OHFe_{0.98}Se$ [29] and $Li_x(NH_3)_yFe_2Se_2$ [30] with thick spacer layers. The result can be understood by the
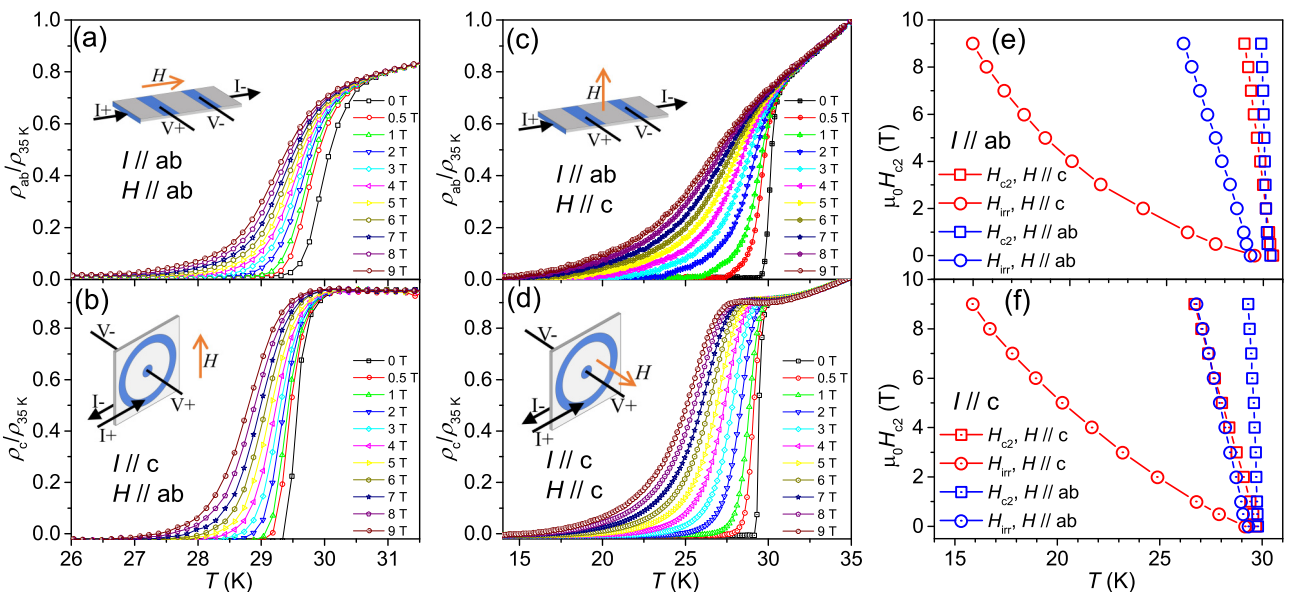
FIG. 3. Temperature and field dependence of the in-plane and out-of-plane normalized resistivity for $CsCa_2Fe_4As_4F_2$ single crystals with external magnetic field parallel to the ab plane (a) and (b) and along the c axis (c) and (d). (e) and (f) The upper critical field (H_{c2}) and the irreversible field (H_{irr}) that are extracted from the $\rho_{ab}(T, H)$ and $\rho_c(T, H)$, respectively.

quasi-2D Fermi-surface sheets revealed by the first-principles calculations [9,10,12].

Impressively, the $\rho_c(T)$ curve shows a broad hump at around 140 K, reminiscent of the metal-to-nonmetal crossover in other layered metals, such as Sr_2RuO_4 [31,32], $NaCo_2O_4$ [33], and $(Bi_{1-x}Pb_x)_2M_3Co_2O_y$ (M = Ba or Sr) [34,35]. A similar behavior was also reported in the electron-doped $Li_x(NH_3)_yFe_2Se_2$ [30] as well as in the cuprate superconductor $Tl_2Ba_2CaCu_2O_8$ [36]. The metal-to-nonmetal crossover is mostly explained in terms of incoherent hopping because of $l_c \leqslant d_{inter}$ (l_c is the electron mean free path along the c axis and d_{inter} is the interbilayer distance). The metal-to-nonmetal crossover of $\rho_c(T)$ in $CsCa_2Fe_4As_4F_2$ could also be associated with the change in the electronic state and in the mobile carrier density because the $\rho_{ab}(T)$ exhibits a round shape at around 150 K. Nevertheless, no significant change in carrier density was observed in the temperature range, according to the Hall coefficient measurements on the sister compounds $KCa_2Fe_4As_4F_2$ and $RbGd_2Fe_4As_4O_2$ [4,6]. These results suggest that the semiconductinglike $\rho_c(T)$ behavior at the high temperatures is most likely due to the interlayer incoherent hopping.

Figure 2(c) magnifies the superconducting transition in ρ_{ab} and ρ_c. One sees that the onset transition temperature (T_c^{onset}) in ρ_{ab} and ρ_c is different. According to the criterion of 90% ρ_n, where ρ_n is the extrapolated normal-state resistivity at T_c, the T_c^{onset} values for ρ_{ab} and ρ_c are 30.5 and 29.8 K, respectively. Meanwhile, the zero-resistance temperatures are basically the same ($T_c^{zero} = 29.4$ K) for ρ_{ab} and ρ_c. The T_c values of the two samples were checked to be the same (29.4 ± 0.1 K) by dc magnetic susceptibility measurement. Also note that the measurements of $\rho_{ab}(T)$ and $\rho_c(T)$ were carried out simultaneously on the same sample puck and, at every temperature, the data were not read until holding for 30 s. Moreover, measurements on additional samples produced similar data (see Fig. S3 in the SM). Therefore, the result (higher T_c^{onset} for ρ_{ab}) is intrinsic, which suggests significant 2D superconducting fluctuations above the bulk T_c.

Figures 3(a)–3(d) show the superconducting transitions in ρ_{ab} and ρ_c under magnetic fields parallel to the ab planes and the c axis, respectively. In all cases, expectedly, the superconducting transitions shift to lower temperatures with increasing magnetic field. Nevertheless, details of the suppression of superconductivity are distinct for different field directions. There are pronounced resistive tails for $H \parallel c$ [Figs. 3(c) and 3(d)]. This is mainly because, for $H \parallel c$, the pancakelike vortices easily flow within ab planes due to the Lorentz force, giving rise to the flux-flow resistance. By contrast, the Josephson-like vortices under $H \parallel ab$ tend to be intrinsically pinned by the insulating spacer layers, hence the flux-flow resistance is very much reduced. Taken 90% and 1% of ρ_n (ρ_n is the extrapolated normal-state resistivity at T_c) as the criteria, respectively, for determining the upper critical field $H_{c2}(T)$ and the irreversible field $H_{irr}(T)$, the resultant $H_{c2}(T)$ and $H_{irr}(T)$ were extracted and plotted in Figs. 3(e) and 3(f). The large gaps (symbols in red) between $H_{c2}^{\perp}(T)$ and $H_{irr}^{\perp}(T)$ dictate a large area of a possible vortex liquid phase in the H-T phase diagram, akin to the scenario in many cuprate superconductors [37]. In comparison, the gaps (symbols in blue) between $H_{c2}^{\parallel}(T)$ and $H_{irr}^{\parallel}(T)$ are much narrower.

In general, $H_{c2}(T)$ nearby T_c is dominantly limited by an orbital pair-breaking effect [38], hence the initial slope of $H_{c2}(T)$ gives information of orbitally limited upper critical field, $H_{c2}^{orb}(T)$. Note that the fluctuation effect is significant in the resistive transition of ρ_{ab}, as described above, we thus only use the $H_{c2}(T)$ data extracted from ρ_c. The initial slopes of $H_{c2}^{\parallel}(T)$ and $H_{c2}^{\perp}(T)$ are given to be -18.2 and -2.9 T/K, respectively, by using a linear fit (note that the $\mu_0(dH_{c2}^{\parallel}/dT)|_{T_c}$ value is very close to that of the $RbGd_2Fe_4As_4O_2$ polycrystals [6]). These slopes allow us to estimate the orbitally limited upper critical fields at zero temperature with the formula $\mu_0H_{c2}^{orb}(0) = -0.73T_c(\mu_0dH_{c2}/dT)|_{T_c}$ in clean limit [39] (the in-plane electron mean free path satisfies $l_{ab} \gg \xi_{ab}$ [22]). Then the anisotropic coherence lengths can be derived using the Ginzburg-Landau (GL) relations $\mu_0H_{c2}^{\perp}(0) = \Phi_0/[2\pi\xi_{ab}^2(0)]$ and $\mu_0H_{c2}^{\parallel}(0) = \Phi_0/[2\pi\xi_{ab}(0)\xi_c(0)]$, where Φ_0 is the magnetic-flux quantum (2.07×10^{-15} Wb). The $\xi_{ab}(0)$ and $\xi_c(0)$ are calculated to be 22.9 and 3.6 Å, respectively. The resulted $\xi_c(0)$ is significantly lower than the interbilayer distance $d_{inter} = 8.597(4)$ Å [5], which indicates that $CsCa_2Fe_4As_4F_2$ is actually a quasi-2D superconductor.

From the initial slopes of H_{c2} for the two field directions, one obtains the anisotropic ratio $\Gamma_{H_{c2}} = H_{c2}^{\parallel}/H_{c2}^{\perp} = 6.3$, at $T \to T_c$. The $\Gamma_{H_{c2}}$ value is obviously larger than those of most FeSCs [20,21]. In general, the anisotropy of H_{c2} means the difference in the effective mass of carriers moving within and across the ab planes, m_{ab} and m_c. According to the GL theory [37], $\Gamma_{H_{c2}} = \sqrt{m_c/m_{ab}}$, then the effective-mass anisotropic ratio is $\Gamma_m = 40$. The result is qualitatively consistent with the quasi-2D characteristic in the electronic structure [12]. The d_{xy} (d_{z^2}) orbital contributes most (least) for the electronic state at the Fermi energy, suggesting an enhanced electronic-structure anisotropy in the hole-doped 12442-type material. Nevertheless, the Γ_m value is still much lower than the Γ_ρ at T_c. A similar discrepancy is seen in $Li_x(NH_3)_yFe_2Se_2$ [30]. Here we note that the formula $\Gamma_{H_{c2}} = \sqrt{m_c/m_{ab}}$ only holds in a single-band scenario with coherent electronic states. For $CsCa_2Fe_4As_4F_2$, there are ten bands crossing the Fermi energy [12]. What is more, the metal-to-nonmetal crossover in $\rho_c(T)$ suggests that only a small portion of charge carriers are in a coherent state for the c-direction transport. Therefore, the inequality $\Gamma_\rho \gg \Gamma_m$ could be allowed in the present system.

It is worth noting that the normal-state $\rho_c(T)$ under $H \parallel c$ shows noticeable negative magnetoresistance near T_c. The resistivity under $\mu_0H = 7$ T is about 1.5% lower than the zero-field resistivity. Furthermore, $\rho_c(T)$ shows a weak upturn under a strong field when temperature approaches T_c. The two phenomena are seemingly contradictory, which needs to be clarified in the future.

C. Magnetic properties

Figure 4(a) shows the temperature dependence of dc magnetic susceptibility of the $CsCa_2Fe_4As_4F_2$ single crystal, measured under a magnetic field of 10 Oe parallel to the ab planes and the c direction. The crystal's dimension is $A \times B \times C = 1.2 \times 1.8 \times 0.030$ mm^3, and the short edge is along the crystallographic c axis. For $H \parallel c$ (along the C edge), the demagnetization factor is calculated to be $N_d^{\perp} = 0.939$
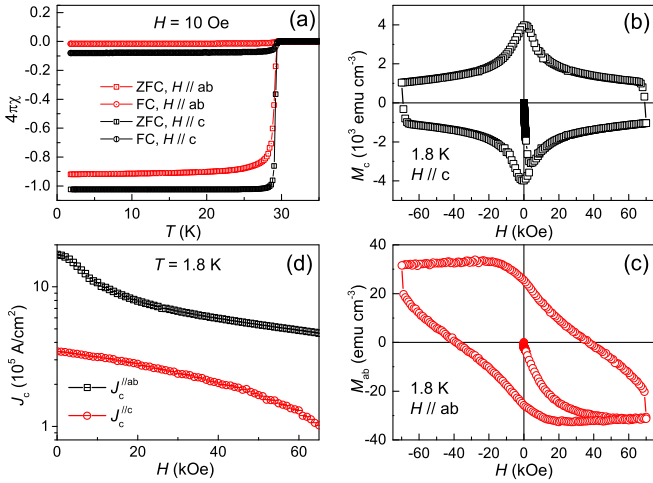
FIG. 4. (a) Temperature dependence of magnetic susceptibility of a $CsCa_2Fe_4As_4F_2$ single crystal under a magnetic field of $H = 10$ Oe parallel to the *ab* planes and the *c* direction in field-cooling (FC) and zero-field-cooling (ZFC) modes. (b) and (c) Isothermal magnetization loops at 1.8 K for $H \parallel c$ and $H \parallel ab$, respectively. (d) Field dependence of in-plane and interplane superconducting critical currents at 1.8 K.

the nearly perfect diamagnetism demonstrates that the single crystal is of high quality. Note that the reduced diamagnetism in the field-cooling (FC) mode is due to a magnetic-flux pinning effect. The flux pinning is more obvious for $H \parallel ab$.

Figures 4(b) and 4(c) show the isothermal magnetization of the identical sample at 1.8 K for the two field directions, respectively. The magnetic-flux pinning effect is confirmed from the remarkable hysteresis loops from which one can estimate the critical current using Bean critical state model [41]. First, the in-plane critical current density $J_c^{\parallel}(H)$ can be calculated by the formula $J_c^{\parallel}(H) = 20\Delta M_c(H)/[A(1 - A/3B)]$, where $\Delta M_c(H)$ is the magnetization difference at a certain magnetic field parallel to the *c* direction. Second, the situation for $H \parallel ab$ is somewhat complicated because of the vortex motions both across and within the planes, which leads to two components for the current density, $J_c^{\perp}(H)$ and $J_c^{\parallel}(H)$. Nevertheless, $J_c^{\perp}$ can still be estimated by $J_c^{\perp}(H) \approx 20\Delta M_{ab}(H)/C$ [42], in the case of $A, B \gg (C/3)J_c^{\parallel}(H)/J_c^{\perp}(H)$ [the result is self-consistent, as shown in Fig. 4(d)]. Under zero field, $J_c^{\parallel}$ and $J_c^{\perp}$ achieve 1.71×10^6 and 3.45×10^5 A/cm², respectively. Even under a strong external field at $H = 70$ kOe, $J_c^{\parallel}$ and $J_c^{\perp}$ remain to be as high as 4.65×10^5 and 1.02×10^5 A/cm², respectively. These J_c values are comparable to those of other iron-based superconducting thin films [20], suggesting potential applications at low temperatures, akin to the case of Bi-based cuprate superconductors [37]. The temperature dependence of the anisotropic critical current density $J_c^{\parallel}(H)$ and $J_c^{\perp}(H)$ are plotted in Fig. S5 in the SM. $J_c^{\parallel}(H)$ declines much faster than $J_c^{\perp}(H)$ with increasing temperature, suggesting much weaker pinning forces for $H \parallel c$ at high temperatures. The result coincides with those of $\rho_c(T, H)$ and $\rho_{ab}(T, H)$ above.

Figure 5(a) displays the $M(H)$ curves at different temperatures from 1.8 to 30 K for $H \parallel c$. In the low-field regions

with a rectangular prism approximation [40], while for $H \parallel ab$ (along the *A* edge), $N_d^{\parallel} = 0.0367$. With the demagnetization correction made, the volume fractions of magnetic shielding, measured in the zero-field-cooling (ZFC) mode, approximate 92% and 102% for $H \parallel ab$ and $H \parallel c$, respectively (exceeding 100% is due to the uncertainties of measurements including those of the sample's dimension). The diamagnetic transition occurs at 29.4 K, in agreement with the T_c^{zero} in the resistivity measurement. The sharp diamagnetic transition as well as

FIG. 5. Measurements of the anisotropic lower critical fields (H_{c1}) in $CsCa_2Fe_4As_4F_2$. (a) and (d) Field dependence of magnetization at various temperatures for $H \parallel c$ and $H \parallel ab$. The dashed lines show the linear fit in the low-field regions. (b) and (e) The deviation of each $M(H)$ curve from the linear fit for $H \parallel c$ and $H \parallel ab$, respectively. The dashed lines are the criteria for determining H_{c1}. (c) and (f) The extracted and corrected (see the text for details) H_{c1} for $H \parallel c$ and $H \parallel ab$, respectively. The data fittings with different models are given in (c).

(say, $H < 10$ Oe), the M-H relation is essentially linear, as represented by the black dashed line (here we call the Meissner line). Deviations from the Meissner line dictate the field penetration into the interior of the sample, and the lower critical field (H_{c1}) can thus be determined [43,44]. Figure 5(b) shows the deviation in magnetization ΔM_c obtained by subtracting the Meissner line from the original $M(H)$ data. We chose a criterion of $\Delta M_c = 5 \times 10^{-5}$ emu, equivalent to 0.59 Oe after taking into account the demagnetization effect, for the determination of $H_{c1}^{\perp *}$. Those $H_{c1}^{\perp *}$ were corrected with $H_{c1}^{\perp} = H_{c1}^{\perp *}/(1 - N_d)$ where $N_d = 0.939$ for $H \| c$. The corrected $H_{c1}^{\perp}(T)$ data are displayed in Fig. 5(c). The zero-temperature value is $H_{c1}^{\perp}(0) = 720$ Oe, which is close to the related hole-doped superconductor $Ba_{0.6}K_{0.4}Fe_2As_2$ [43].

$H_{c1}^{\perp}(T)$ data may give information on the superconducting gap [43,45]. We tried to fit the above $H_{c1}^{\perp}(T)$ result considering two simple scenarios, (1) single s-wave-gap model and (2) two s-wave-gap model. $H_{c1}(T)$ relates the normalized superfluid density $\rho_s(T)$ as [45]

$$\frac{H_{c1}(T)}{H_{c1}(0)} = \rho_s = 1 + 2 \int_\Delta^\infty dE \frac{\partial f}{\partial E} \frac{E}{\sqrt{E^2 - \Delta(t)^2}}, \quad (2)$$

where $f(E)$ is Fermi function and t is the reduced temperature T/T_c. The temperature dependence of the BCS-like gap $\Delta(t)$ can be approximated as $\Delta(t) = \Delta_0 \tanh\{1.82[1.018(1/t - 1)]^{0.51}\}$, where $\Delta(0)$ denotes the zero-temperature isotropic gap. In the two-gap scenario, the superfluid density is treated as a linear summation, $\rho_s = w\rho_s(\Delta_1) + (1 - w)\rho_s(\Delta_2)$ with a weighting factor w.

The fitting result is shown in Fig. 5(c). Obviously the two-gap model better meets the experimental data. The fitted parameters are: $\Delta_1(0) = 2.61k_BT_c = 6.75$ meV, $\Delta_2(0) = 0.90k_BT_c = 2.32$ meV, and $w = 0.44$. The contribution of each superconducting gap is also presented in Fig. 5(c), revealing how the single-gap model fails to catch the experimental data. The conclusion of two superconducting gaps in $CsCa_2Fe_4As_4F_2$ is basically consistent with the very recent heat transport study on the single crystals [46] and muon-spin-rotation (μSR) results with the polycrystalline samples [13,14], although the latter suggest that a nodal gap should be involved. Here we cannot distinguish whether the small gap is isotropic or with nodes by the fitting. Note that the μSR measurements [13,14] employed the polycrystalline samples with a lower T_c, which could give rise to the difference.

The in-plane penetration depth λ_{ab} can be estimated with the formula $\mu_0 H_{c1}^{\perp} = \Phi_0/(4\pi\lambda_{ab}^2)[\ln\kappa_c + 0.5]$, where $\kappa_c = \lambda_{ab}/\xi_{ab}$. With $\xi_{ab}(0) = 22.9$ Å, $\lambda_{ab}(0) = 986$ Å, and $\kappa_c = 43$ given. The $\lambda_{ab}(0)$ value is about 40% of that derived from the μSR measurement [14] primarily because of polycrystalline samples employed [note that $\lambda_c(0)$ is much larger]. One may further estimate the 2D Ginzburg number $Gi^{2D} = k_BT_c/(\sqrt{2}\varepsilon_0 d)$, where d refers to the thickness of the superconducting layers (here we take $d \approx 8$ Å) and $\varepsilon_0 = \Phi_0/(4\pi\lambda_{ab})^2$. The resulted Gi^{2D} is 0.013, which is significantly larger than those of most FeSCs [19], yet smaller than those of the layered Bi- and Tl-based superconductors [27,28,37]. Since Gi^{2D} quantifies the strength of 2D superconducting thermal fluctuations, the enhanced T_c^{onset} for $\rho_{ab}(T)$ is then naturally understood.

TABLE I. Anisotropic superconducting parameters of the $CsCa_2Fe_4As_4F_2$. Conventional notations and definitions are used.

Parameters	Values (unit)
$\mu_0 \frac{dH_{c2}^{\|}}{dT}\|_{T_c}$	-18.2 (T/K)
$\mu_0 \frac{dH_{c2}^{\perp}}{dT}\|_{T_c}$	-2.9 (T/K)
$\mu_0 H_{c2}^{\|,orb}(0)$	396 (T)
$\mu_0 H_{c2}^{\perp,orb}(0)$	63 (T)
$\frac{H_{c2}^{\|}}{H_{c2}^{\perp}}\|_{T_c}$	6.3
$\xi_{ab}(0)$	22.9 (Å)
$\xi_c(0)$	3.6 (Å)
κ_{ab}	751
κ_c	43
$\lambda_{ab}(0)$	986 (Å)
$\lambda_c(0)$	47 200 (Å)

We also measured the isothermal magnetization curves of the $CsCa_2Fe_4As_4F_2$ crystal under $H \| ab$, which are shown in Fig. 5(d). Different from the $M_c(H)$ curves, the $M_{ab}(H)$ data exhibit nonmonotonic field dependence, reminiscence of the so-called fishtail effect in relation with the vortex dynamics [47,48]. Here we only deal with the lower critical field for $H \| ab$, as what we did for $H_{c1}^{\perp}$. The criterion used for the determination of $H_{c1}^{\| *}$ is $\Delta M_{ab} = 3 \times 10^{-6}$ emu, equivalent to 0.56 Oe. The corrected $H_{c1}^{\|}$ is close to the $H_{c1}^{\| *}$ because of the small demagnetization factor. Figure 5(f) displays the temperature dependence of $H_{c1}^{\|}$. Noticeably, $H_{c1}^{\|}(T)$ shows a maximum at around 8 K, which is very unusual for general temperature dependence of H_{c1}. Note that the recent μSR experiment suggests an unknown magnetic phase that appears at about 8 K [14], which could be the reason for the slight descending of $H_{c1}^{\|}(T)$.

The zero-temperature $H_{c1}^{\|}(0)$ extrapolated is about 25 Oe, much lower than the $H_{c1}^{\perp}(0)$ value, which also reveals the strong anisotropy in $CsCa_2Fe_4As_4F_2$. The interplane penetration depth λ_c can be calculated with the relation $\mu_0 H_{c1}^{ab} = \Phi_0/(4\pi\lambda_{ab}\lambda_c)[\ln\kappa_{ab} + 0.5]$, where $\kappa_{ab} = \sqrt{\lambda_{ab}\lambda_c}/\sqrt{\xi_{ab}\xi_c}$. The resulted κ_{ab} and $\lambda_c(0)$, together with κ_c and $\lambda_{ab}(0)$, are summarized in Table I for brevity. The extremely large $\lambda_c(0)$ indicates that a very low superfluid density along the c direction, consistent with the quasi-2D nature of the title material.

IV. CONCLUDING REMARKS

In conclusion, we have successfully grown single crystals of $CsCa_2Fe_4As_4F_2$, a recently discovered FeSC with separate double Fe_2As_2 layers. With the electrical and magnetic measurements we found that the material is strongly anisotropic, evidenced by the following data. (1) The anisotropic resistivity ratio is an order of $\sim10^3$, and the $\rho_c(T)$ and $\rho_{ab}(T)$ data show contrasting behaviors. (2) $\rho_{ab}(T)$ shows a broadened superconducting transition with a higher T_c^{onset}. (3) In the superconducting state near T_c, the anisotropic ratio of H_{c2} is 6.3, which is higher than most FeSCs. (4) The anisotropic ratio of $H_{c1}(0)$ is as high as 29. (5) The dimensionless 2D Ginzburg

number achieves 0.013. All these parameters suggest quasi-2D characteristic in $CsCa_2Fe_4As_4F_2$. The result conversely implies that the 2D Fe_2As_2 layers (including separate double Fe_2As_2 layers) play an important role in the emergence of superconductivity in FeSCs.

The giant anisotropy and the consequent 2D superconducting thermal fluctuations are scarcely observed in FeSCs, making the title material unique for studying the anisotropic superconductivity including the vortex dynamics. The uniqueness might be associated with the crystal structure containing separate double Fe_2As_2 layers. The special crystal structure yields the electronic structure with six hole-type cylindrical Fermi-surface sheets and four electron-type ones, all of which are very two dimensional [12]. While a two-gap model well explains the temperature dependence of the lower critical field, it is of interest for the future to further clarify which bands are responsible for superconductivity in the 12442-type system.

[1] D. C. Johnston, The puzzle of high temperature superconductivity in layered iron pnictides and chalcogenides, Adv. Phys. **59**, 803 (2010).

[2] H. Jiang, Y.-L. Sun, Z.-A. Xu, and G.-H. Cao, Crystal chemistry and structural design of iron-based superconductors, Chin. Phys. B **22**, 087410 (2013).

[3] H. Hosono and K. Kuroki, Iron-based superconductors: Current status of materials and pairing mechanism, Physica C **514**, 399 (2015).

[4] Z.-C. Wang, C.-Y. He, S.-Q. Wu, Z.-T. Tang, Y. Liu, A. Ablimit, C.-M. Feng, and G.-H. Cao, Superconductivity in $KCa_2Fe_4As_4F_2$ with separate double Fe_2As_2 layers, J. Am. Chem. Soc. **138**, 7856 (2016).

[5] Z. Wang, C. He, Z. Tang, S. Wu, and G. Cao, Crystal structure and superconductivity at about 30 K in $ACa_2Fe_4As_4F_2$ (A = Rb, Cs), Sci. China Mater. **60**, 83 (2017).

[6] Z.-C. Wang, C.-Y. He, S.-Q. Wu, Z.-T. Tang, Y. Liu, A. Ablimit, Q. Tao, C.-M. Feng, Z.-A. Xu, and G.-H. Cao, Superconductivity at 35 K by self doping in $RbGd_2Fe_4As_4O_2$, J. Phys.: Condens. Matter **29**, 11LT01 (2017).

[7] Z.-C. Wang, C.-Y. He, S.-Q. Wu, Z.-T. Tang, Y. Liu, and G.-H. Cao, Synthesis, Crystal structure and superconductivity in $RbLn_2Fe_4As_4O_2$ (Ln = Sm, Tb, Dy, and Ho), Chem. Mater. **29**, 1805 (2017).

[8] S.-Q. Wu, Z.-C. Wang, C.-Y. He, Z.-T. Tang, Y. Liu, and G.-H. Cao, Superconductivity at 33–37 K in $ALn_2Fe_4As_4O_2$ (A = K and Cs; Ln = lanthanides), Phys. Rev. Mater. **1**, 044804 (2017).

[9] J. Ishida, S. Iimura, and H. Hosono, Effects of disorder on the intrinsically hole-doped iron-based superconductor $KCa_2Fe_4As_4F_2$ by cobalt substitution, Phys. Rev. B **96**, 174522 (2017).

[10] G. Wang, Z. Wang, and X. Shi, Self-hole-doping-induced superconductivity in $KCa_2Fe_4As_4F_2$, Europhys. Lett. **116**, 37003 (2016).

[11] Z. Wang, G. Wang, and X. Tian, Electronic structure and magnetism of $RbGd_2Fe_4As_4O_2$, J. Alloys Compd. **708**, 392 (2017).

[12] B. Singh and P. Kumar, Unconventional iron-based superconductor $CsCa_2Fe_4As_4F_2$: A first-principle study, AIP Conf. Ser. **1953**, 120019 (2018).

[13] M. Smidman, F. K. K. Kirschner, D. T. Adroja, A. D. Hillier, F. Lang, Z. C. Wang, G. H. Cao, and S. J. Blundell, Nodal multigap superconductivity in $KCa_2Fe_4As_4F_2$, Phys. Rev. B **97**, 060509(R) (2018).

[14] F. K. K. Kirschner, D. T. Adroja, Z.-C. Wang, F. Lang, M. Smidman, P. J. Baker, G.-H. Cao, and S. J. Blundell, Two-gap superconductivity with line nodes in $CsCa_2Fe_4As_4F_2$, Phys. Rev. B **97**, 060506(R) (2018).

[15] D. T. Adroja, F. K. K. Kirschner, F. Lang, M. Smidman, A. D. Hillier, Z.-C. Wang, G.-H. Cao, G. B. G. Stenning, and S. J. Blundell, Multigap superconductivity in $RbCa_2Fe_4As_4F_2$ investigated using μSR measurements, J. Phys. Soc. Jpn. **87**, 124705 (2018).

[16] Y. Li, Z. C. Wang, G. H. Cao, J. M. Zhang, B. Zhang, T. Wang, H. Pang, F. S. Li, and Z. W. Li, Mössbauer spectroscopy study of magnetic fluctuations in superconducting $RbGd_2Fe_4As_4O_2$, Physica C **548**, 21 (2018).

[17] B. Wang, Z.-C. Wang, K. Ishigaki, K. Matsubayashi, T. Eto, J. Sun, J.-G. Cheng, G.-H. Cao, and Y. Uwatoko, Pressure-induced enhancement of superconductivity and quantum criticality in the 12442-type hybrid-structure superconductor $KCa_2Fe_4As_4F_2$, Phys. Rev. B **99**, 014501 (2019).

[18] J. P. Sun, Z. C. Wang, Z. Y. Liu, S. X. Xu, T. Eto, Y. Sui, B. S. Wang, Y. Uwatoko, G. H. Cao, and J. G. Cheng, Effect of pressure on the self-hole-doped superconductor $RbGd_2Fe_4As_4O_2$, J. Phys.: Condens. Matter **31**, 044001 (2018).

[19] M. Putti, I. Pallecchi, E. Bellingeri, M. R. Cimberle, M. Tropeano, C. Ferdeghini, A. Palenzona, C. Tarantini, A. Yamamoto, J. Jiang, J. Jaroszynski, F. Kametani, D. Abraimov, A. Polyanskii, J. D. Weiss, E. E. Hellstrom, A. Gurevich, D. C. Larbalestier, R. Jin, B. C. Sales, A. S. Sefat, M. A. McGuire, D. Mandrus, P. Cheng, Y. Jia, H. H. Wen, S. Lee, and C. B. Eom, New Fe-based superconductors: Properties relevant for applications, Supercond. Sci. Technol. **23**, 034003 (2010).

[20] H. Hosono, A. Yamamoto, H. Hiramatsu, and Y. Ma, Recent advances in iron-based superconductors toward applications, Mater. Today **21**, 278 (2018).

[21] J.-l. Zhang, L. Jiao, Y. Chen, and H.-q. Yuan, Universal behavior of the upper critical field in iron-based superconductors, Frontiers Phys. **6**, 463 (2011).

[22] See Supplemental Material at http://link.aps.org/supplemental/10.1103/PhysRevB.99.144501 which contains six sections: I. Chemical composition analysis; II. SEM microscopy; III. x-ray diffraction rocking curve; IV. Anisotropic resistivity measurements; V. Anisotropic critical current density; and VI. Electron mean free path.

[23] M. A. Albedah, F. Nejadsattari, Z. M. Stadnik, Y. Liu, and G.-H. Cao, Mössbauer spectroscopy measurements on the 35.5 K superconductor $Rb_{1-\delta}EuFe_4As_4$, Phys. Rev. B **97**, 144426 (2018).

[24] M. Rotter, M. Pangerl, M. Tegel, and D. Johrendt, Superconductivity and crystal structures of $(Ba_{1-x}K_x)Fe_2As_2$ ($x = 0$–1), Angew. Chem. Int. Ed. **47**, 7949 (2008).

[25] X. F. Wang, T. Wu, G. Wu, H. Chen, Y. L. Xie, J. J. Ying, Y. J. Yan, R. H. Liu, and X. H. Chen, Anisotropy in the Electrical Resistivity and Susceptibility of Superconducting $BaFe_2As_2$ Single Crystals, Phys. Rev. Lett. **102**, 117005 (2009).

[26] M. A. Tanatar, N. Ni, G. D. Samolyuk, S. L. Bud'ko, P. C. Canfield, and R. Prozorov, Resistivity anisotropy of AFe_2As_2 ($A = Ca$, Sr, Ba): Direct versus Montgomery technique measurements, Phys. Rev. B **79**, 134528 (2009).

[27] S. Martin, A. T. Fiory, R. M. Fleming, G. P. Espinosa, and A. S. Cooper, Vortex-Pair Excitation Near the Superconducting Transition of $Bi_2Sr_2CaCu_2O_8$ Crystals, Phys. Rev. Lett. **62**, 677 (1989).

[28] V. Hardy, A. Maignan, C. Martin, F. Warmont, and J. Provost, Anisotropy of resistivity in Tl-based single crystals: Direct evidence for the influence of the blocking-layer thickness and correlation with superconducting properties, Phys. Rev. B **56**, 130 (1997).

[29] X. Dong, K. Jin, D. Yuan, H. Zhou, J. Yuan, Y. Huang, W. Hua, J. Sun, P. Zheng, W. Hu, Y. Mao, M. Ma, G. Zhang, F. Zhou, and Z. Zhao, $(Li_{0.84}Fe_{0.16})OHFe_{0.98}Se$ superconductor: Ion-exchange synthesis of large single-crystal and highly two-dimensional electron properties, Phys. Rev. B **92**, 064515 (2015).

[30] S. Sun, S. Wang, R. Yu, and H. Lei, Extreme anisotropy and anomalous transport properties of heavily electron doped $Li_x(NH_3)_yFe_2Se_2$ single crystals, Phys. Rev. B **96**, 064512 (2017).

[31] Y. Maeno, H. Hashimoto, K. Yoshida, S. Nishizaki, T. Fujita, J. G. Bednorz, and F. Lichtenberg, Superconductivity in a layered perovskite without copper, Nature (London) **372**, 532 (1994).

[32] K. Yoshida, Y. Maeno, S. Nishizaki, S. Ikeda, and T. Fujita, Crossover from 3D to 2D metallic conduction in Sr_2RuO_4, J. Low Temp. Phys. **105**, 1593 (1996).

[33] I. Terasaki, Y. Sasago, and K. Uchinokura, Large thermoelectric power in $NaCo_2O_4$ single crystals, Phys. Rev. B **56**, R12685 (1997).

[34] S. M. Loureiro, D. P. Young, R. J. Cava, R. Jin, Y. Liu, P. Bordet, Y. Qin, H. Zandbergen, M. Godinho, M. Núñez-Regueiro, and B. Batlogg, Enhancement of metallic behavior in bismuth cobaltates through lead doping, Phys. Rev. B **63**, 094109 (2001).

[35] I. Tsukada, T. Yamamoto, M. Takagi, T. Tsubone, S. Konno, and K. Uchinokura, Ferromagnetism and large negative magnetoresistance in Pb doped BiSrCoO misfit-layer compound, J. Phys. Soc. Jpn. **70**, 834 (2001).

[36] J.-P. Salvetat, H. Berger, A. Halbritter, G. Mihály, D. Pavuna, and L. Forró, Crossovers in the out-of-plane resistivity of superconducting $Tl_2Ba_2CaCu_2O_8$ single crystals, Europhys. Lett. **52**, 584 (2000).

[37] G. Blatter, M. V. Feigel'man, V. B. Geshkenbein, A. I. Larkin, and V. M. Vinokur, Vortices in high-temperature superconductors, Rev. Mod. Phys. **66**, 1125 (1994).

[38] G. H. Cao and Z. W. Zhu, Superconductivity with peculiar upper critical fields in quasi-one-dimensional Cr-based pnictides, Chin. Phys. B **27**, 107401 (2018).

[39] E. Helfand and N. R. Werthamer, Temperature and purity dependence of the superconducting critical field, H_{c2}. II, Phys. Rev. **147**, 288 (1966).

[40] A. Aharoni, Demagnetizing factors for rectangular ferromagnetic prisms, J. Appl. Phys. **83**, 3432 (1998).

[41] C. P. Bean, Magnetization of high-field superconductors, Rev. Mod. Phys. **36**, 31 (1964).

[42] E. M. Gyorgy, R. B. van Dover, K. A. Jackson, L. F. Schneemeyer, and J. V. Waszczak, Anisotropic critical currents in $Ba_2YCu_3O_7$ analyzed using an extended Bean model, Appl. Phys. Lett. **55**, 283 (1989).

[43] C. Ren, Z.-S. Wang, H.-Q. Luo, H. Yang, L. Shan, and H.-H. Wen, Evidence for Two Energy Gaps in Superconducting $Ba_{0.6}K_{0.4}Fe_2As_2$ Single Crystals and the Breakdown of the Uemura Plot, Phys. Rev. Lett. **101**, 257006 (2008).

[44] M. Abdel-Hafiez, J. Ge, A. N. Vasiliev, D. A. Chareev, J. Van de Vondel, V. V. Moshchalkov, and A. V. Silhanek, Temperature dependence of lower critical field $H_{c1}(T)$ shows nodeless superconductivity in FeSe, Phys. Rev. B **88**, 174512 (2013).

[45] A. Carrington and F. Manzano, Magnetic penetration depth of MgB_2, Physica C **385**, 205 (2003).

[46] Y. Y. Huang, Z. C. Wang, Y. J. Yu, J. M. Ni, Q. Li, E. J. Cheng, G. H. Cao, and S. Y. Li, Multigap nodeless superconductivity in $CsCa_2Fe_4As_4F_2$ probed by heat transport, Phys. Rev. B **99**, 020502(R) (2019).

[47] M. Jirsa, L. Půst, D. Dlouhý, and M. R. Koblischka, Fishtail shape in the magnetic hysteresis loop for superconductors: Interplay between different pinning mechanisms, Phys. Rev. B **55**, 3276 (1997).

[48] S. Salem-Sugui, L. Ghivelder, A. D. Alvarenga, L. F. Cohen, K. A. Yates, K. Morrison, J. L. Pimentel, H. Luo, Z. Wang, and H.-H. Wen, Flux dynamics associated with the second magnetization peak in the iron pnictide $Ba_{1-x}K_xFe_2As_2$, Phys. Rev. B **82**, 054513 (2010).